Magnetic ground state of the one-dimensional ferromagnetic chain compounds $M(NCS)_2(thiourea)_2$ ($M = $ Ni, Co)

S. P. M. Curley, R. Scatena, R. C. Williams, P. A. Goddard, P. Macchi, T. J. Hicken, T. Lancaster, F. Xiao, S. J. Blundell, V. Zapf, J. C. Eckert, E. H. Krenkel, J. A. Villa, M. L. Rhodehouse, and J. L. Manson

Magnetic ground-state of the one-dimensional ferromagnetic chain compounds $M(\mathbf{NCS})_2(\mathbf{thiourea})_2$; $M = \mathbf{Ni, Co.}$

S. P. M. Curley,[1] R. Scatena,[2, 3] R. C. Williams,[1] P. A. Goddard,[1, *] P. Macchi,[4, 5, 3]

T. J. Hicken,[6] T. Lancaster,[6] F. Xiao,[7] S. J. Blundell,[8] V. Zapf,[9] J. C. Eckert,[10]

E. H. Krenkel,[10] J. A. Villa,[11] M. L. Rhodehouse,[11] and J. L. Manson[11, †]

[1]*Department of Physics, University of Warwick, Gibbert Hill Road, Coventry, CV4 7AL, UK*

[2]*Department of Physics, Clarendon Laboratory, University of Oxford, Parks Rd., Oxford, OX1 3PU, United Kingdom*

[3]*Department of Chemistry and Biochemistry, University of Bern, 3012 Bern, Switzerland*

[4]*Department of Chemistry, Materials, and Chemical Engineering, Polytechnic of Milan, Milan 20131, Italy*

[5]*Istituto Italiano di Tecnologia, Center for Nano Science and Technology CNST@polimi, Milan 20133, Italy*

[6]*Durham University, Department of Physics, South Road, Durham, DH1 3LE, United Kingdom*

[7]*Laboratory for Neutron Scattering and Imaging,*
Paul Scherrer Institut, CH-5232 Villigen PSI, Switzerland

[8]*Department of Physics, Clarendon Laboratory, University of Oxford,*
Parks Road, Oxford, OX1 3PU, United Kingdom

[9]*National High Magnetic Field Laboratory, Materials Physics and Applications Division,*
Los Alamos National Laboratory, Los Alamos, New Mexico 87545, USA

[10]*Physics Department, Harvey Mudd College, Claremont, CA, United States*

[11]*Department of Chemistry and Biochemistry, Eastern Washington University, Cheney, Washington 99004, USA*

The magnetic properties of the two isostructural molecule-based magnets, $Ni(NCS)_2(thiourea)_2$, $S = 1$, [thiourea = $SC(NH_2)_2$] and $Co(NCS)_2(thiourea)_2$, $S = 3/2$, are characterised using several techniques in order to rationalise their relationship with structural parameters and ascertain magnetic changes caused by substitution of the spin. Zero-field heat capacity and muon-spin relaxation measurements reveal low-temperature long-range ordering in both compounds, in addition to Ising-like ($D < 0$) single-ion anisotropy ($D_{Co} \sim$ -100 K, $D_{Ni} \sim$ -10 K). Crystal and electronic structure, combined with DC-field magnetometry, affirm highly quasi-one-dimensional behaviour, with ferromagnetic intrachain exchange interactions $J_{Co} \approx +4$ K and $J_{Ni} \sim +100$ K and weak antiferromagnetic interchain exchange, on the order of $J' \sim -0.1$ K. Electron charge and spin-density mapping reveals through-space exchange as a mechanism to explain the large discrepancy in J-values despite, from a structural perspective, the highly similar exchange pathways in both materials. Both species can be compared to the similar compounds $MCl_2(thiourea)_4$, $M = Ni(II)$ (DTN) and Co(II) (DTC), where DTN is known to harbour two magnetic field-induced quantum critical points. Direct comparison of DTN and DTC with the compounds studied here shows that substituting the halide Cl^- ion, for the NCS^- ion, results in a dramatic change in both the structural and magnetic properties.

INTRODUCTION

Constraining magnetic moments to lie and interact in one-dimensional chains or two-dimensional planes has, over the years, been an area of continued interest within the magnetism community [1–3]. The reduced dimensionality generally serves to enhance quantum fluctuations, leading to the material hosting an array of exotic quantum ground states [4, 5]. Several classes of low-dimensional materials can exhibit an order to disorder transition driven by an external tuning parameter, such as magnetic field, that pushes the system though a quantum critical point (QCP) [6, 7].

Considering the case of one-dimensional (1D) materials, a notable system is the ferromagnetically coupled effective $S = 1/2$ chain material $CoNb_2O_6$. Applying a magnetic field transverse to Co(II) Ising-axis pushes the system through a QCP, as it moves from a ferromagnetic (FM) ordered ground-state to a disordered quantum paramagnetic phase [8, 9]. The existence of a QCP in 1D chains is not exclusive to the case of FM coupling.

The $S = 1$ antiferromagnetic (AFM) chain material $NiCl_2(thiourea)_4$ (DTN), where thiourea = $SC(NH_2)_2$, passes through two field-induced QCPs, at least one of which belongs to the universality class of a Bose-Einstein Condensate (BEC) [10, 11].

In terms of physically realising such systems, the use of organic ligands has proven highly effective in constructing crystal architectures that readily promote low-dimensional magnetic behaviour [12–16]. A selection of recently published materials showcase the ability to test the limits of the theoretical understanding of $S = 1/2$ and $S = 1$ chain materials [17–19]. To achieve quasi-one-dimensional (Q1D) behaviour, the choice of intrachain bridging-ligand is a decisive one, as it ultimately determines the sign and strength of the intrachain exchange interaction (J). Non-bridging ligands also play an important role in promoting Q1D behaviour, keeping adjacent chains well separated and mitigating interactions due to interchain exchange (J') [15, 16]. Characterising both J and J' is therefore paramount to establish how the crystal structure influences the magnetism in Q1D sys-

tems. The ultimate goal of this work is to move toward the construction of bespoke magnetic materials, where the magnetic properties can be chemically tuned from the point of synthesis. The work also provides an avenue to study how structural properties influence the observed ground-state, and possible emergence of quantum-critical behaviour, in low-dimensional magnetic systems.

We therefore turned our attention to the two isostructural coordination polymers $Co(NCS)_2(thiourea)_2$, $S = 3/2$, and the $S = 1$ analogue $Ni(NCS)_2(thiourea)_2$. Despite both compounds being first synthesised some time ago [20–22] we present here the first comprehensive study of their magnetic properties. The isostructural architecture of the two compounds, outlined below, permits us to investigate the effect the choice of transition metal ion has upon both the sign and strength of J and J', both of which govern the dimensionality of the system. An additional reason to study the properties of these materials is to establish their connection to known, chemically similar quantum magnets, such as the 1D chain DTN [23]. In the chosen materials the transition metal ion (M) sits in a distorted MS_4N_2 octahedral environment, pictured in Figure 1(a), suggesting the compounds likely possess a non-zero single-ion anisotropy (SIA) parameter (D) and rhombic anisotropy term (E). Along the crystallographic a-axis, adjacent M-ions form chains through sulphide ions on two thiourea molecules forming two S-bridge pathways as shown in Figure 1(b). The M—S—M bond angles are close to $90°$, therefore, according to the Goodenough-Kanamori rules [24, 25], these chain compounds represent promising platforms to investigate Q1D FM behaviour. The magnetic properties of both compounds within an applied magnetic field ($\mu_0 H$) can be summarised by the following Hamiltonian,

$$\mathcal{H} = -J \sum_{<i,j>} \hat{\mathbf{S}}_i \cdot \hat{\mathbf{S}}_j - J' \sum_{<i,j'>} \hat{\mathbf{S}}_i \cdot \hat{\mathbf{S}}_{j'} + D \sum_i (\hat{\mathbf{S}}_i^z)^2$$
$$+ E \sum_i [(\hat{\mathbf{S}}_i^x)^2 - (\hat{\mathbf{S}}_i^y)^2] + \mu_B \mu_0 \sum_i \mathbf{H} \cdot \mathbf{g} \cdot \hat{\mathbf{S}}_i, \quad (1)$$

where $\hat{\mathbf{S}}_i$ is the spin of each ion i, $< i, j >$ denotes a sum over nearest neighbours and a primed index in the summation describes the interaction with a nearest neighbour in an adjacent chain; $J > 0$ corresponds to FM interactions. Here, $\mathbf{g} = \text{diag}(g_x, g_y, g_z)$ is a tensor of g-factors where diagonal components are not necessarily equal. Whilst the triclinic structure of both materials are permissive of an E-term, the equatorial MS_4 environment (discussed in detail below) are only slightly distorted. As the departure from octahedral symmetry is limited, any E-term is expected to be small, as observed in similar Ni(II) and Co(II) complexes [26–28].

Several methods were employed to investigate the electronic and magnetic properties of the two compounds in an attempt to ascertain the sign and magnitude of the dominant terms in Eq. 1: J, J', and D. To identify likely magnetic exchange pathways, both crystal and electronic structures were inspected using multipolar model refinement of high resolution single-crystal X-ray diffraction data. Chemical bonding analysis was performed on the electron charge density distributions obtained from X-ray diffraction and density functional theory (DFT) calculations, and compared with calculated spin density maps to highlight the role of the magnetic ions. Heat capacity combined with muon-spin relaxation measurements revealed magnetic ordering and elucidated the magnitude of the SIA. DC-field magnetometry measurements, in combination with DFT calculations of the exchange coupling constants, helped illustrate a coherent picture of the magnetic ground state.

RESULTS

Crystal structure

Crystallisation of $Co(NCS)_2(thiourea)_2$ and $Ni(NCS)_2(thiourea)_2$ coordination polymers resulted in needle-shaped single-crystals where single-crystal X-ray diffraction (SCXRD) measurements revealed twinning in both. $Co(NCS)_2(thiourea)_2$ could however also be obtained with thin-sheet morphology; these crystals showed clean single-crystal diffraction frames. Needle-like $Ni(NCS)_2(thiourea)_2$ crystals were irremediably affected by twinning and attempts to re-crystallise different morphologies proved unsuccessful. Both compounds crystallise into a triclinic structure with the space-group $P\bar{1}$, selected structural refinement parameters are listed in Table SIV of the supplemental information (SI) see [29] (as are the experimental details).

High quality $Co(NCS)_2(thiourea)_2$ single-crystals allowed X-ray diffraction data to be collected up to $d_{\min} = 0.50$ Å, which, in combination with low-temperatures ($T = 100$ K), allowed the refinement of the crystal structure, but also of the aspherical electron-charge density distribution, presented below. The Co atom resides on an inversion centre and lies in the middle of an octahedron built by pairs of Co—N [2.0226(4) Å], Co—S [2.5523(1) Å], and Co—S [2.5972(1) Å] coordination bonds. As a result of these bond lengths, the octahedral environment is axially compressed along the N—Co—N axis. The S—Co—S angles within the equatorial plane [84.19(1)° and 95.81(1)°] and the angle between the octahedron axis and the equatorial plane [96.56(1)°] show the Co(II) octahedra are slightly distorted. A Co—S—Co angle of 95.81(1)° defines the geometry of the two Co—S—Co bridges that make up the polymeric chain. The polymeric chains are packed together in the bc-plane by H-bonds in the range $3.43 - 3.47$ Å and classify as weakly interacting.

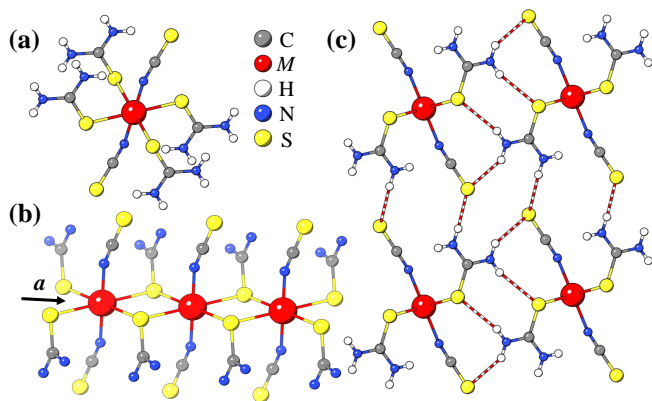Single-crystal X-ray diffraction data for

FIG. 1. Structure of $M(NCS)_2(thiourea)_2$ where $M = Ni^{2+}$, Co^{2+}. (a) Local M^{2+} octahedral environment. (b) Two M—S—M bonds form bibridge chains that propagate along the crystallographic a-axis. (c) H-bonding (striped-bonds) between adjacent chains within the bc-plane. The structure is shown for $M = Co^{2+}$ at $T = 100$ K.

$Ni(NCS)_2(thiourea)_2$ was measured at $T = 173$ K up to $d_{min} = 0.70\,\text{Å}$ with a second twinning component of $27.7(1)\%$ observed in the crystal. Analogous to the structure of $Co(NCS)_2(thiourea)_2$, the Ni atom sits on the inversion centre in the middle an octahedron built by two of each Ni—N [$1.997(2)$ Å], Ni—S [$2.5069(6)$ Å], and Ni—S [$2.5517(6)$ Å] coordination bonds. The S—Ni—S angles within the equatorial plane [$83.93(2)°$ and $96.07(2)°$] and the angle between the octahedron axis and the equatorial plane [$97.20(7)°$] also show a slight distortion to the Ni(II) octahedra. A Ni—S—Ni angle of $96.07(2)°$ defines the geometry of two Ni—S—Ni bridges along the polymeric chain. H-bonds pack the chains in the bc-plane with distances between the donor and acceptor within the range $3.43 - 3.45$ Å, which again classify as weakly bonded.

The experimentally-determined structural parameters of $Co(NCS)_2(thiourea)_2$ and $Ni(NCS)_2(thiourea)_2$ are very similar to one another. This similarity is found also from periodic DFT optimisation of the measured geometries, Table SVI [29], which returned an even tighter correspondence between bond lengths and angles in the two species.

Muon-spin relaxation

Zero-field positive-muon-spin-relaxation (ZF μ^+SR) measurements on $M(NCS)_2(thiourea)_2$ were performed, with example spectra spanning the measured temperature range as shown in Figure 2. The spectra measured for $Co(NCS)_2(thiourea)_2$ show no oscillations in the asymmetry, but consist of two exponentially relaxing components, one with a large relaxation rate, found to
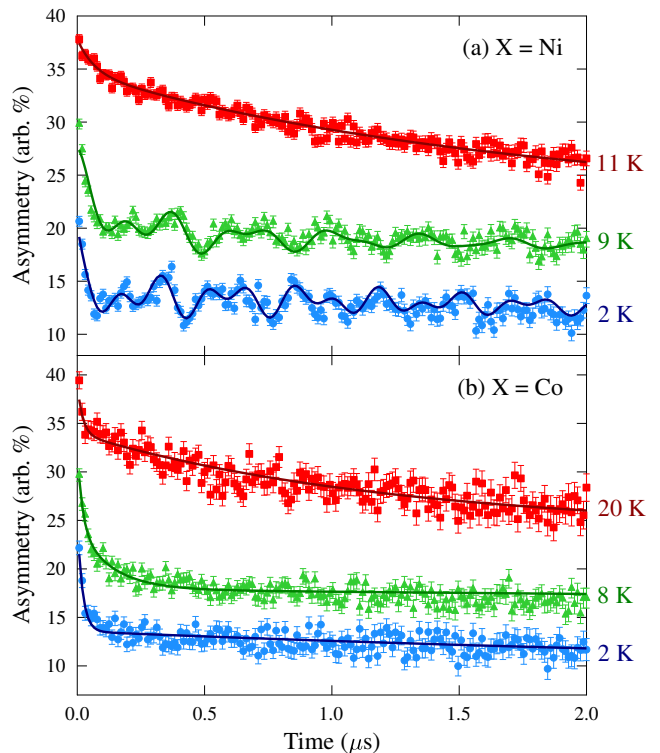

FIG. 2. ZF μ^+SR spectra measured on (a) $Ni(NCS)_2(thiourea)_2$ and (b) $Co(NCS)_2(thiourea)_2$. Data is presented with a vertical offset where needed for clarity. Fits shown as detailed in the Supplemental Material [29]

be constant over the entire temperature range, and one with a smaller relaxation rate that dominates at later times; see SI [29] and [30] for fit details. The large relaxation rate is often observed in coordination polymers of this type and has been ascribed to a class of muon sites that are not well coupled to the magnetism (hence its temperature independence) that are realised close to electron density (e.g. double bonds, aromatic rings etc.) [31, 32].

The temperature evolution of the smaller relaxation rate (λ_1) is shown in Figure 3. It exhibits a peak around 8 K, indicating a phase transition from a magnetically ordered to disordered state, in good agreement with heat-capacity and magnetometry measurements discussed below. The lack of oscillations at low temperature and the observed exponential relaxation suggest that the system is dominated by dynamic fluctuations on the muon timescale, such that coherent precession of the muon-spin is not measured. This has been noted in several coordination polymer magnets containing Fe^{2+} [33], Mn^{2+} [34] and (in some cases) Ni^{2+} [35], where the sizeable magnetic moment can lead to a large, fluctuating distribution of local magnetic fields at the muon sites. (In contrast, coordination polymer magnets containing Cu^{2+} often show oscillations in the ordered regime [31].) The
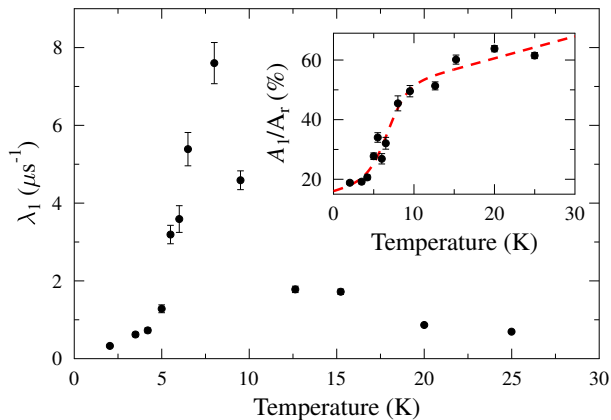
FIG. 3. Temperature evolution of the small relaxation rate (λ_1) extracted through fitting ZF μ^+SR asymmetry spectra measured on Co(NCS)$_2$(thiourea)$_2$. Inset shows the temperature evolution of the ratio of the amplitude of the component with small relaxation rate (A_1) to the total relaxing asymmetry (A_r). Line is a guide to the eye.

FIG. 4. Temperature evolution of the smallest oscillation frequency (ν_1) observable in the ZF μ^+SR asymmetry spectra measured on Ni(NCS)$_2$(thiourea)$_2$, with a fit to Eqn. 2. Inset shows the temperature evolution of the total relaxing asymmetry (A_{rel}) from the same measurements.

observed exponential relaxation suggests that the sample is in the fast-fluctuation regime below T_c, where the relaxation rate varies as $\lambda \propto \Delta^2 \tau$. Here Δ is the variance of the field distribution sampled by the muons and τ is the fluctuation time. The variance Δ varies with the size of the local magnetic field, so we might expect materials with larger moments to lead to larger relaxation rates. In this scenario the relaxation rate will scale faster with moment than the oscillation frequency, and therefore a higher moment could prevent the observation of coherent precession. This could explain the observed lack of oscillations in this system compared to similar materials with smaller moments. It is also possible that the lack of oscillations reflects a greater propensity for Co-based systems to adopt magnetic structures that yield inhomogeneous local field distributions or that give dynamic fluctuations in the muon (MHz) timeframe.

Further evidence for a transition around 8 K comes from the rapid change in amplitude of the small relaxation rate component (A_1), as shown in the inset of Figure 3. (This effect has also been observed in similar materials close to the transition temperature [33–35].) Significant in this case is that both this change and the peak in λ persist over a relatively wide range of temperature, extending at least 2–3 K below T_c. This suggests that the phase transition is extended in temperature on the MHz timescale with an onset of dynamics occurring in the ordered regime above 5 K.

In contrast to the Co material, ZF μ^+SR spectra for Ni(NCS)$_2$(thiourea)$_2$ show oscillations in the asymmetry for temperatures $T \lesssim 10.4$ K, indicating coherent muon-spin precession consistent with long-range magnetic order. Two oscillation frequencies [in constant ratio
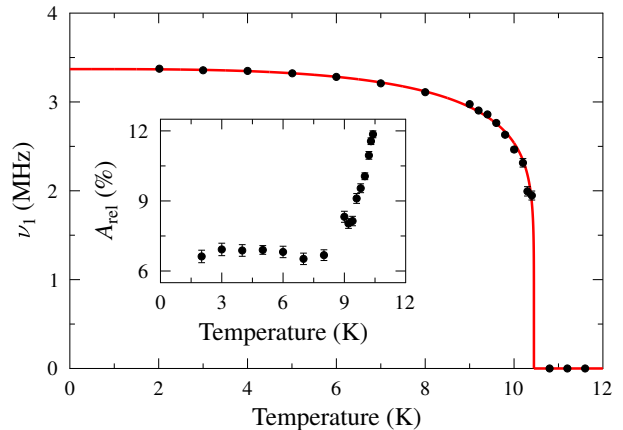
$\nu_2/\nu_1 = 1.754(1)$] were observable over the whole temperature range, with a third $\nu_3 \simeq 3\nu_1$ only observable for $T \lesssim 7$ K. This indicates three distinct muon stopping sites in this material.

By fitting these spectra as seen in Figure 2(b), see SI [29] for fit details, the frequencies were extracted. The smallest frequency was fitted to

$$\nu_i(T) = \nu_i(0)\left[1 - \left(\frac{T}{T_N}\right)^\delta\right]^\beta, \qquad (2)$$

as seen in Figure 4. It was found that $\nu_1(0) = 3.37(2)$ MHz [corresponding to a local magnetic field of 24.1(1) mT at the muon-spin site at zero-temperature], $\delta = 3.2(3)$, $\beta = 0.14(3)$ and $T_N = 10.4(1)$ K. This value of β is consistent with a system dominated by 2D magnetic fluctuations, being very close to the value for the 2D Ising model, $\beta = 1/8$ [36]. This transition temperature is also supported by the behaviour of relaxation rates of the oscillating components, which both show a peak between $T = 10.3$ K and $T = 10.4$ K. These rates diverge when approached from below, indicating critical slowing down of magnetic fluctuations, which often occurs in the proximity of a magnetic transition.

The disappearance of the third frequency, in combination with the increase in the relaxing asymmetry (A_{rel}) for $T \gtrsim 7$ K, seen in the inset of Figure 4, is evidence for the onset of the magnetic transition in this material, suggesting again, a broad phase transition taking place in the region $7 \lesssim T \lesssim 10.4$ K on the muon timescale. For $T \gtrsim 10.4$ K no oscillations are observable in the asymmetry spectra, consistent with the system being magnetically disordered.

Heat capacity

Zero-field heat capacity (C) was measured as a function of temperature for a single-crystal of $Co(NCS)_2(thiourea)_2$ and a polycrystalline pressed pellet of $Ni(NCS)_2(thiourea)_2$. In order to isolate the low-temperature magnetic heat capacity (C_{mag}) the high-temperature ($T \gtrsim 30$ K) contribution was reproduced using a phenomenological model containing both Debye and Einstein phonon modes and subtracted as a background [29, 37]. For both compounds, a λ-peak in C_{mag} at low-temperatures, seen in Figure 5(a), is indicative of a transition to a magnetically-ordered state, giving ordering temperatures of $T_c = 6.82(5)$ K and 10.5(1) K for the Co and Ni species, respectively, in excellent agreement with ZF μ^+SR.

$Co(NCS)_2(thiourea)_2$ C_{mag} data possesses a notably sharper λ-peak compared to $Ni(NCS)_2(thiourea)_2$. Single-crystal magnetometry for the Co species, discussed below, provides the reason for this. The magnetometry data indicate an AFM ground-state, where the spins possess a strong Ising-like SIA. For a Q1D chain of Ising spins, a broad-hump in C_{mag} is expected as the reduced dimensionality causes the build up of spin-spin correlations at temperatures above the transition temperature [38, 39]. The sharp nature of the peak points to 2D or 3D Ising-like long range ordering within the material. The measured response of $C_{mag}(T)$ was not well captured by simulations of $C_{mag}(T)$ for the 2D Ising model [40, 41]; Figure S2 [29]. This would imply the secondary exchange along b and c are similar in magnitude, which is also supported by the DFT calculations (below) and indicates $n' = 4$ next nearest neighbours.

The magnetic entropy per mole (S_{mag}) for both compounds can be determined using,

$$S_{mag}(T) = \int_0^T dT' \frac{C_{mag}(T')}{T'}, \qquad (3)$$

where it is assumed $C_{mag} = 0$ at $T = 0$ K. The results are shown in the inset of Figure 5(a). For $Ni(NCS)_2(thiourea)_2$, S_{mag} fully recovers to $R\ln(3)$ (R is the ideal gas constant) as expected for a $S = 1$ ion. In contrast, $Co(NCS)_2(thiourea)_2$ shows an initial sharp upturn before a broad rise to a plateau at $R\ln(2)$ around 30 K. Electronic structure calculations reveal the Co ion sits in the high-spin Co^{2+} state. The spin configuration consists of two Kramer-doublets split by an energy-gap of magnitude $2D$ [see Figure 5(b)]. For a $S = 3/2$ ion, we expect S_{mag} to recover to $R\ln(4)$ in accordance with $R\ln(2S+1)$. A recovery to $R\ln(2)$ is indicative of a system exhibiting large SIA which keeps the two Kramer-doublets well separated as illustrated in Figure 5(b), suggesting that the system can be well approximated using an effective spin-half approach within the low-temperature regime. We therefore expect $D \sim -100$ K
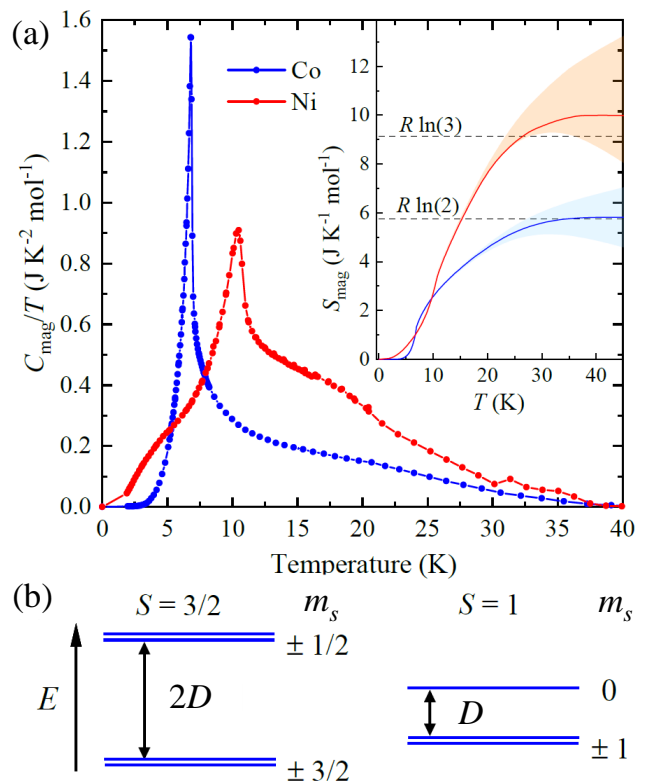

FIG. 5. (a) Zero-field magnetic heat capacity (C_{mag}) divided by temperature (T) and plotted as a function of T. Inset shows the resultant magnetic entropy (S_{mag}), where the shaded regions are representative of errors introduced by the uncertainty in the amplitudes of the high-temperature fit components. (b) Energy (E) level diagrams for $S = 3/2$ and $S = 1$ moments within octahedral environments with easy-axis single-ion anisotropy ($D < 0$) where m_s is the eigenvalue of the spin operator S_z.

as seen in similar easy-axis Co(II) complexes [28].

The behaviour of the Ni-species was investigated further by measuring C_{mag} in applied magnetic fields up to 9 T as shown in Figure 6. The λ-peak is initially suppressed in field, suggesting the ground-state is AFM in nature. At higher fields, the ordering peak ceases to be resolvable and the broad hump shifts to higher temperatures reflecting the Schottky-like response to the field induced Zeeman splitting of the ground-state energy levels. The inset of Figure 5 shows S_{mag} fully recovers to $R\ln(3)$ on warming above about 40 K in zero field and 50 K at 9 T, indicating the level splitting is completely overcome by these temperatures. This is consistent with $|D| \sim 10$ K, which is typical for Ni^{2+} ions in similar local environments [42, 43].

Magnetometry

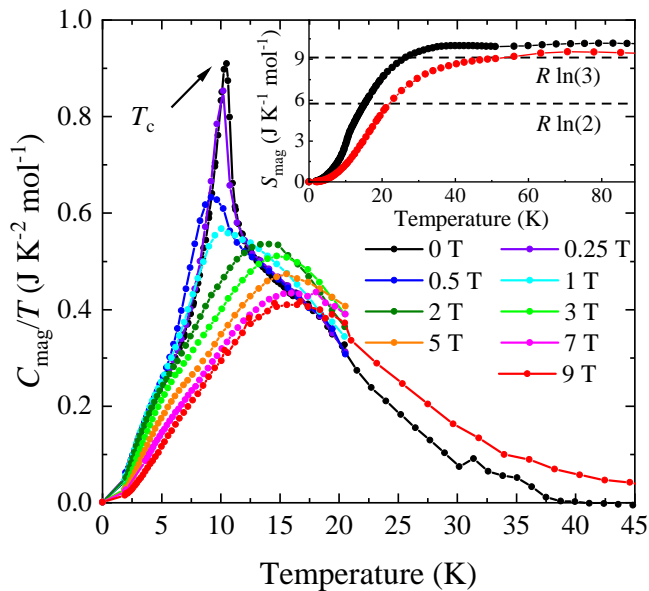Single-crystal magnetometry measurements were performed on $Co(NCS)_2(thiourea)_2$ with the external

FIG. 6. Magnetic heat capacity (C_{mag}) divided by temperature (T) and plotted as a function of T for a polycrystalline pressed pellet of Ni(NCS)$_2$(thiourea)$_2$ measured in applied fields up to 9 T. The zero-field transition temperature to a magnetically ordered state is indicated at T_c. Inset shows magnetic entropy (S_{mag}) recover to $R\ln(3)$ at 0 and 9 T, as expected for a $S = 1$ ion.

magnetic-field applied along three orthogonal orientations: parallel to the chain axis a, perpendicular to a within the ab-plane denoted b' and normal to the ab-plane denoted c'. The angle between the magnetic field and the unique N—Co—N axis is 84° for $\mu_0 H \parallel a$, 73° for $\mu_0 H \parallel b'$ and 18° for $\mu_0 H \parallel c'$.

Figure 7(a) shows that upon decreasing temperature, the magnetic susceptibility $[\chi(T)]$ for field along all three orientations rises to a sharp peak before plateauing at low-temperatures, behaviour indicative of an AFM ground state. The Fisher relation [44] estimates a transition temperature $T_c = 6.7(1)$ K, in excellent agreement with heat capacity and μ^+SR data. The $\chi(T)$ with field parallel to c', red circles Figure 7(a), is an order of magnitude greater than measurements made with the field along a or b', verifying a strong Ising-like ($D < 0$) SIA. Due to the close proximity of c' to the unique axial N—Co—N bond, it is highly likely that the magnetic moments on the Co ions are co-linear with the N—Co—N axis.

The $\chi^{-1}(T)$ data for all three field directions, inset Figure 7(a), shows curvature persisting up to the highest measured temperature ($T = 300$ K). This non-Curie-like behaviour suggests that the leading energy term in the Hamiltonian is similar in size to the thermal energy in this temperature range. On the basis of our heat capacity measurements, we expect this term to be D. Thus we estimate $|D| \sim 100$ K in agreement with heat capacity
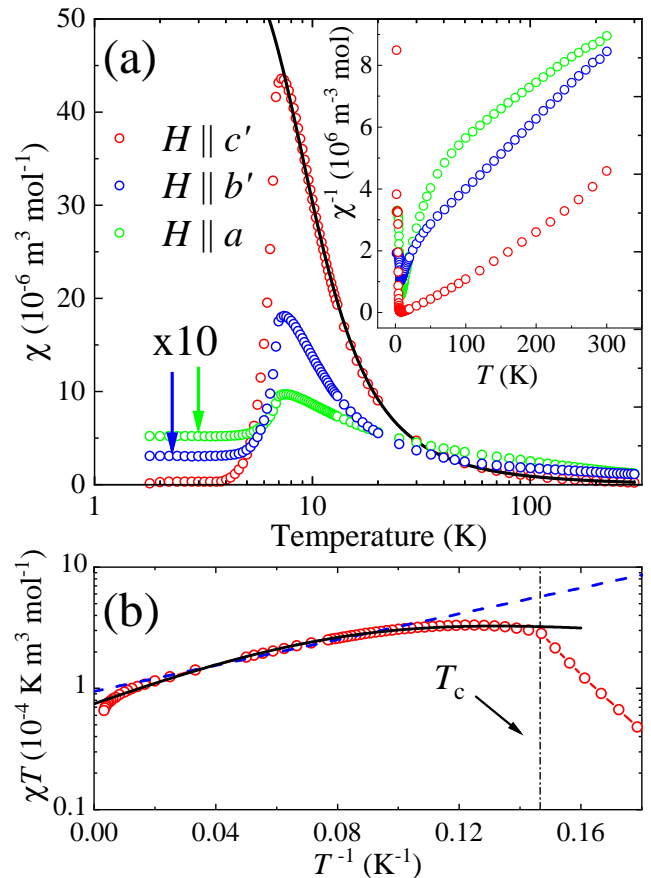

FIG. 7. Single-crystal magnetic susceptibility $\chi(T)$ data for Co(NCS)$_2$(thiourea)$_2$ measured at $\mu_0 H = 0.1$ T. (a) $\chi(T)$ for different field directions where data for $H \parallel b'$ and a are multiplied by a factor of 10. Inset shows a plot of $\chi^{-1}(T)$ with no scaling. (b) Semi-logarithmic plot of $\chi T(T)$ against T^{-1} (discussed in text) for field parallel to c'. Dashed line is a fit to $\chi_{1D}^{\parallel}$ (see text). Solid line in both panels is a fit to Eq. 4 within the temperature range 10 K $\leq T \leq$ 100 K.

data and similar Co(II) complexes [28].

The large negative SIA (zero-field splitting = $2|D| \sim$ 100 K) suggests that as temperature is lowered below 100 K, a vanishingly small proportion of the spins will populate the excited doublet and the magnetic properties can be accounted for within an effective spin-half ($S_{eff} = 1/2$) Ising model. This means that over the temperature range $10 \leq T \leq 100$ K, the susceptibility for $H \parallel c'$ (which is close to parallel to the expected Ising axis) can be approximated by that of the ideal 1D $S = 1/2$ Ising chain $[\chi_{1D}^{\parallel}(T)]$ and parameterised by J_{eff}, the primary exchange energy in the effective $S_{eff} = 1/2$ picture [45, 46]. Deviations from strictly 1D behaviour can be accounted for by introducing a mean-field correction to the susceptibility given by the expression [46],

$$\chi_{mf} = \frac{\chi_{1D}^{\parallel}(T)}{[1 - (n'J_{eff}')\chi_{1D}^{\parallel}(T)/C_{1D}]}, \quad (4)$$

where C_{1D} is the easy-axis Curie constant for the idealised 1D picture and J'_{eff} is the interchain exchange in the effective $S_{\text{eff}} = 1/2$ picture arising from n' interchain nearest neighbours where $n' = 4$ for this material.

Following the analysis by Greeney *et al.* [46] in Figure 7(b) we show a semi-logarithmic plot of $\chi T(T)$ against T^{-1} for $H \parallel c$. In this diagram $\chi_{1D}^{\parallel}(T)$ is a straight line with gradient given by the intrachain exchange J_{eff} and intercept related to C_{1D}. A positive slope is indicative of FM intrachain exchange ($J_{\text{eff}} > 0$). The sharp kink at T_c indicates the onset of long-range order. The data near T_c deviates from the linear response predicted by the ideal 1D Ising model (dashed line). A fit to Eq. 4 within the temperature range $10\,\text{K} \leq T \leq 100\,\text{K}$ ($T < 2|D|$, well within the $S_{\text{eff}} = 1/2$ regime) is found to more accurately track the data [solid line, Figure 7 (a-b)], indicating the importance of the intrachain exchange interactions. The fit to Eq. 4 returned parameters of $g_{\text{eff}} = 8.0(1)$, $J_{\text{eff}} = 10.4(2)\,\text{K}$ and $J'_{\text{eff}} = -0.31(2)\,\text{K}$. The fit parameters are consistent with the effective $S = 1/2$ model, in which the full Co(II) moment of the ground state doublet is absorbed into the effective g-factor and exchange energies. The real exchange, J, is related to the effective value via $J = (3/5)^2 J_{\text{eff}}$ [47, 48], hence the values we extract are $J = 3.62(7)\,\text{K}$ and $J' = -0.12(1)\,\text{K}$. The fit to Eq. 4 deviates from the data near the onset of long-range order. The departure at high temperatures is caused by the breakdown of the Ising model as temperatures approach $|D| \sim 100\,\text{K}$. The difference between $\chi(T)$ for the field along b' and a may be due to either, the existence of a small E-term, a slight misalignment of the magnetic field or different temperature dependencies of the effective magnetic moment along b' and a.

The magnetisation $M(H)$ of Co(NCS)$_2$(thiourea)$_2$ with field parallel to c' is shown in Figure 8. At $T \leq 4\,\text{K}$, the induced moment is approximately zero at low fields before rapidly rising to a saturation moment of $M_{\text{sat}} = 4.1(1)\,\mu_B$ per Co^{2+} ion at $\mu_0 H_{\text{sf}} = 0.29(5)$ T. We attribute this feature to spin-flip behaviour where the spins are rapidly polarised from their AFM ground-state to an FM saturated state as the interchain AFM bonds are overcome by the Zeeman interaction. The step broadens and disappears at $T > 4\,\text{K}$.

Within the $S_{\text{eff}} = 1/2$ model M_{sat} yields $g_{\text{eff}} = 8.2(1)$, in excellent agreement with the result from fitting $\chi(T)$. The field at which the spin-flip occurs can be related to the AFM interaction strength via $g_{\text{eff}}\mu_B\mu_0 H_{\text{sf}} = Sn'J'_{\text{eff}}$. Assuming $n' = 4$, we obtain $J' = -0.3(1)\,\text{K}$ which is in reasonable agreement with the value extracted from $\chi(T)$. As $M(H)$ directly probes the AFM interchain bonds at low-temperature, during the spin-reversal process, we expect $M(H)$ to provide us with the more trustworthy estimate of J'. The inset to Figure 8 shows hysteresis in $M(H)$ for $T < 4\,\text{K}$, expected for FM coupled Ising spins. This behaviour is also observed in the similar FM Ising chain compound Co(NCS)$_2$(4-
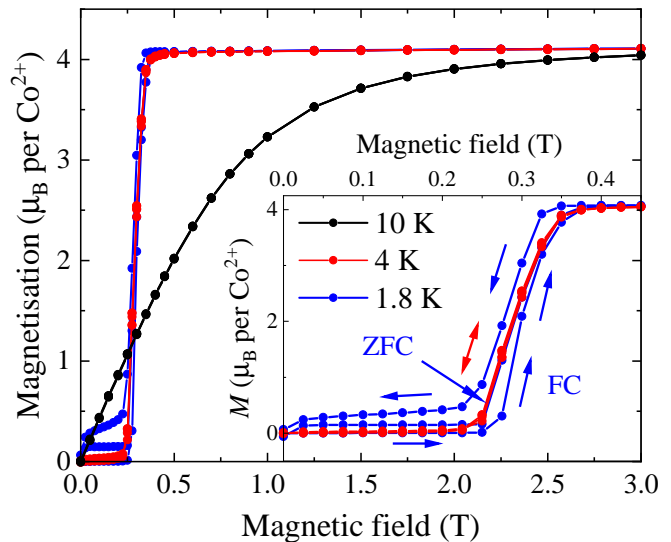

FIG. 8. Single-crystal DC-field magnetisation $M(H)$ data for Co(NCS)$_2$(thiourea)$_2$ with the field parallel to c'. Inset highlights the low-field hysteretic behaviour seen at the lowest temperature. Zero-field cooled (ZFC) and field cooled (FC) up-sweeps are indicated with arrows.

benzoylpyridine)2 (4-benzoylpyridine = C$_{12}$H$_9$NO) [49].

Figure 9(a) shows powder $\chi(T)$ for Ni(NCS)$_2$(thiourea)$_2$. Upon decreasing temperature, $\chi(T)$ rises to a peak before dropping and plateauing at low-temperatures. The inset of Figure 9(a) shows $\chi^{-1}(T)$, where a Curie-Weiss fit for $T \geq 100\,\text{K}$ returns $g = 2.29(1)\,\text{K}$ and $\Theta_{\text{CW}} = +42(1)\,\text{K}$. $\chi T(T)$ data, Figure 9(b), increase on cooling from room temperature, reach a broad maximum and then drop towards zero at $T < 10\,\text{K}$. At high temperature, $\chi T(T)$ data approaches a flat paramagnetic value at $T \approx 300\,\text{K}$, likely plateauing at $T \approx 300 - 400\,\text{K}$. This corresponds to the energy scale of the largest term in the Hamiltonian J, such that $k_B T \approx 2nJ$ ($n = 2$ is the number of nearest neighbours in the chain). This estimates $J \approx 75 - 100\,\text{K}$, in good agreement with DFT calculations below. The Fisher method [44] determines $T_c = 10.4(4)\,\text{K}$, Figure 9(b), in excellent agreement with heat capacity and μ^+SR measurements. These observations are consistent with large FM primary exchange interactions and a considerably smaller secondary AFM exchange, leading to an AFM ground state.

Figure 9(c) shows $M(H)$ for a powder sample of Ni(NCS)$_2$(thiourea)$_2$. At low-fields, $M(H)$ is approximately zero prior to exhibiting a sharp upturn at $\mu_0 H_{\text{sf}} = 0.65(5)$ T which we ascribe to spin-flip behaviour. The rise of $M(H)$ slows at fields ~ 1 T before increasing monotonically above 3 T, approaching $M(H) \sim 2\,\mu_B$ per Ni^{2+} ion at the maximum experimentally accessible field of 7 T. The field at which the spin-flip occurs can be used to estimate the interchain magnetic exchange J'
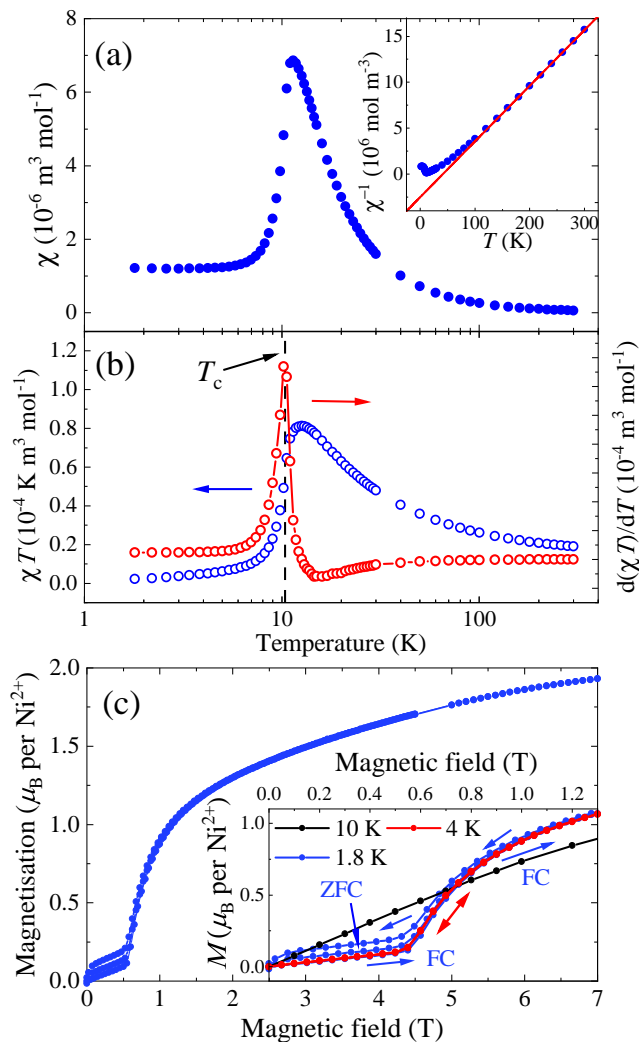
FIG. 9. (a) Powder magnetic susceptibility $\chi(T)$ data for Ni(NCS)$_2$(thiourea)$_2$ measured at $\mu_0 H = 0.1$ T. Inset shows $\chi^{-1}(T)$ fit to the Curie-Weiss model over the temperature range $100 \leq T \leq 300$ K. (b) $\chi(T)$ multiplied by temperature [$\chi T(T)$] (blue, left-axis) and it's derivative (red, right-axis) with critical temperature T_c marked with a dashed line. (c) Powder DC-field magnetisation $M(H)$ for Ni(NCS)$_2$(thiourea)$_2$. Inset shows hysteretic behaviour $T < 4$ K with zero-field cooled (ZFC) and field-cooled (FC) sweeps marked.

via $g\mu_B\mu_0 H_{sf} = 2Sn'J'$ where n' is the number of nearest interchain neighbours [50]. Taking $g = 2.29(1)$, from $\chi^{-1}(T)$, and $n' = 4$ we estimate $J' = 0.13(1)$ K.

The behaviour of $M(H)$ above $\mu_0 H_{sf}$ can be explained by considering the polycrystalline nature of the sample. Grains with their easy-axis parallel to the applied field are those that contribute to the spin-flip. At $\mu_0 H_{sf}$, their spins are rapidly polarised along the field direction. In contrast, grains not orientated with their easy-axis parallel to the field have their spins more slowly polarised along the field direction as the applied field increases.

These spins contribute to the slow rise of $M(H)$ after $\mu_0 H_{sf}$. By 7 T, $M(H)$ approaches ≈ 2 μ_B per Ni^{2+} ion. This is consistent with $M_{sat} \approx 2.29$ μ_B per Ni^{2+} ion as expected from the g-factor extracted from the fit to $\chi^{-1}(T)$. The inset of Figure 9(b) shows hysteretic behaviour in $M(H)$ for $T < 4$ K similar to that observed in Co(NCS)$_2$(thiourea)$_2$.

Calculated exchange coupling constants

In order to help validate the sign and strength of J and J' determined from the magnetometry, the geometries optimised by DFT were used to calculate the magnetic superexchange coupling constants. Along each axis, the energy difference (ΔE) between ferromagnetic (FM) and antiferromagnetic (AFM) coupling was calculated for adjacent M ions and used to obtain the sign and magnitude of the magnetic exchange interaction. As $\Delta E = E_{FM} - E_{AFM}$, $\Delta E < 0$ is representative of AFM exchange. Values of ΔE were converted to exchange coupling by considering a single J convention in the Hamiltonian (sum over unique exchange pathways), the results of these calculations are shown in Table II and Table SII [29]. We find that the primary exchange is FM in both materials, Table II, with $J = 4.22$ K for the Co species and $J = 78.13$ K for the Ni compound (occurring along a, Table SII [29]). Interchain exchange interactions in both compounds are on the order of $|J'| \sim 0.1$ K and shown in Table II. Weak AFM interchain exchange along b is predicted in both compounds with FM exchange along c predicted in the Ni species as outlined in Table SII [29]. Such a discrete change in sign of the exchange is difficult to verify experimentally. Due to the small magnitude of J', and the convergence criterion used for the energy calculations, we note that the calculated J' parameters are less reliable than those calculated for J. In addition, small changes in the lattice geometry can have statistically significant effects on such small energy differences. The calculated J is roughly two and four orders of magnitude greater than J' for Co(NCS)$_2$(thiourea)$_2$ and Ni(NCS)$_2$(thiourea)$_2$ respectively (see Table II); supporting our argument of Q1D behaviour.

Charge and spin density

DFT calculations and magnetometry data both suggest the intrachain exchange in the Co species is significantly weaker than in the Ni species. To investigate the underlying mechanism responsible for the large difference in the values of J, electronic configurations of the M sites, charge density maps, and calculated spin density distributions were estimated; see [29] and [51–54] for details.

High-resolution X-ray diffraction data refined using the

TABLE I. Experimentally (Exp. MM) and calculated (Calc. MM) d-orbitals occupancy for $M(NCS)_2(thiourea)_2$ as estimated from the multipolar model (MM). The z-axis was set along the unique M—N bond whilst the x- and y-axis were set along M—S bonds in the equatorial plane.

d-orbital	$M = $ Co		$M = $ Ni
	Exp. MM	Calc. MM	Calc. MM
z^2	1.06(2)	1.29	1.46
xz	1.34(2)	1.59	2.04
yz	1.87(2)	1.64	2.06
$x^2 - y^2$	1.42(2)	1.30	1.44
xy	1.87(2)	1.63	2.04
tot	7.45(10)	7.47	9.05

Hansen-Coppens multipolar model (MM) [55, 56] was adopted to retrieve the electronic configuration and experimental charge density distribution. The population of the fitted multipolar functions is effectively used to estimate the occupancy of d-isorbitals functions. Results for the Co material, Table I, indicate the ion resides in the high-spin $[t_{2g}^5, e_g^2]$ electronic configuration. The experimental electronic configuration for Co^{2+} in $Co(NCS)_2(thiourea)_2$ was validated by comparison with the MM refinement of the structure factor calculated from DFT [57, 58]. In addition, DFT simulations allowed estimation of the electronic configuration of Ni^{2+} in $Ni(NCS)_2(thiourea)_2$ for which high-resolution X-ray data was not available (Table I). The occupancy of d-orbitals functions suggest that the Ni ion is in the $[t_{2g}^6, e_g^2]$ electronic configuration. In this case, the abundant occupancy of the $d_{x^2-y^2}$ and d_{z^2} orbital functions can be an effect of electron-spin density being partially delocalised onto the ligands. However, an occupancy slightly exceeding the formal one or two electrons is not unusual in MM refinement, since the multipoles are d-orbital shape functions freely refined against the structure factor, where occupancy values tending to two electrons represent fully occupied orbitals. The same issue concerns theoretical calculations that use orbital functions to compute a wavefunction from which individual orbital populations are extracted by projecting the crystal orbitals onto atomic basis, and therefore do not guarantee integer occupancy. Here, for sake of a fair comparison, we adopted the very same kind of projection for experiment and calculations, namely, multipolar expansion refined against measured or computed structure factors.

The valence electron-charge density, responsible for chemical bonding, is shown by deformation density maps in terms of regions of charge density excess and depletion obtained from the difference between multipolar and spherical charge density. The different electronic configurations retrieved for $Co(NCS)_2(thiourea)_2$ and $Ni(NCS)_2(thiourea)_2$ are reflected in their deformation density maps. Figure 10 shows the deformation den-

sity in the equatorial plane (relevant for the intrachain magnetic exchange coupling). In both coordination polymers, the electron density is clearly depleted (dotted red contours) towards the S-ligands, the $d_{x^2-y^2}$ being singularly occupied in both materials. Conversely, there is a clear excess of electron-charge density located around the Ni ion in regions between S-ligands (blue contours) depicting the fully occupied d_{xy}-orbital. The Co ion has a third semi-occupied orbital pointing between the ligands which leads to a reduction in the electron density along this direction, shown in Figure 10(a) as a diminished blue contoured region along the Co $\cdots$ Co (through-space) direction.

Comparing bond lengths alone is not sufficient to establish the equivalence of interactions in isostructural compounds, as different ions have, for instance, different ionic radii which play an important role in defining the strength and nature of the chemical bonds. Therefore, quantum theory of atoms in molecules (QTAIM) [59] was applied to find bond trajectories and analyse the properties of the electron-charge density at the bond critical points (bcp). Thus, electron-density-based bond properties allow us to quantitatively compare chemical bonds. The electron density and its Laplacian at the bcp have equivalent values in corresponding M-ligand interactions Table SV [29], establishing that these interactions are indeed analogous in the two materials. Moreover, these quantities emphasize differences between bonds, $e.g.$, the electron density at the M—N bond critical point is twice that of the M—S bonds confirming strongly anisotropic octahedral environments in both materials. Properties at the $M \cdots M$ bcp are appreciably different, and no bond trajectory and corresponding bcp are found in $Ni(NCS)_2(thiourea)_2$. Some covalent character of the M-ligand interactions is shown by the QTAIM integrated charges in Table SIII [29], where the formal oxidation states of the M^{2+} and NCS^- ions are reduced due to charge sharing in the bonds, a clear sign of deviation from purely ionic interactions. Likewise, a slightly positive charge on the thiourea ligand (formally neutral)
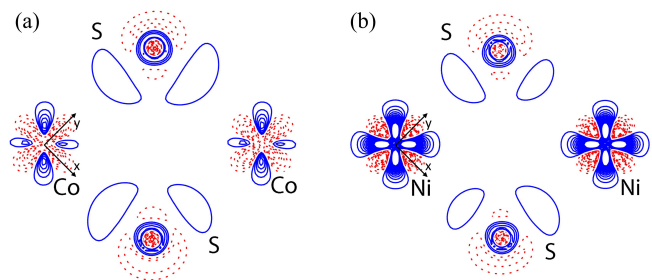

FIG. 10. Deformation electron-density maps for (a) $Co(NCS)_2(thiourea)_2$ and (b) $Ni(NCS)_2(thiourea)_2$. Blue and red contours (0.2 e Å^{-3}) represent regions of electron charge density excess and depletion, respectively.
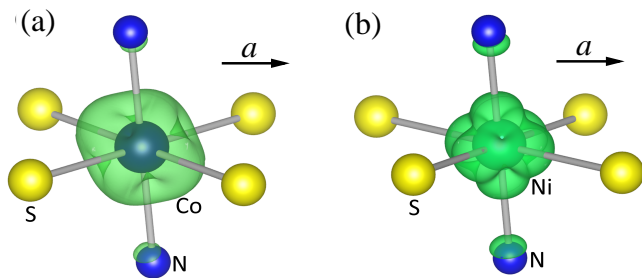
FIG. 11. Calculated spin-density maps for (a) $Co(NCS)_2(thiourea)_2$ and (b) $Ni(NCS)_2(thiourea)_2$ plotted at the isovalue of $0.005\,e$ per $Å^3$. Spin-density regions are outlined as 3D green contours.

is indicative of a ligand to metal σ-donation mechanism.

Electronic configurations and deformation density maps inferred the possible magnetic superexchange pathways in the materials, establishing that in $Co(NCS)_2(thiourea)_2$, a through-space magnetic interaction is available, whereas in $Ni(NCS)_2(thiourea)_2$ it is absent. The calculated electron spin-density distributions for the two compounds follow explicitly the differences in their electronic configurations. In $Co(NCS)_2(thiourea)_2$, the calculated spin-density distribution, centred around the Co ion, is quite spherical as shown in Figure 11(a). Here, the spin-density is concentrated not only towards the ligands but also directly along the a-axis, permitting two possible exchange pathways between adjacent Co ions: a through-bond interaction along the two Co—S—Co bridges and a through-space $Co \cdots Co$ exchange interaction. The latter must be AFM as it is a result of bond-formation which is subject to the Pauli exclusion principle. In contrast, the spin-density at the Ni sites is polarised only along the ligands, see Figure 11(b). In this case, the spin-density is concentrated exclusively along the Ni—S—Ni pathways and towards the Ni—N bond. Therefore, $Ni(NCS)_2(thiourea)_2$ can only exploit the Ni—S—Ni through-bond interactions and, unlike $Co(NCS)_2(thiourea)_2$, has no through-space magnetic exchange.

DISCUSSION

Table II shows the values of J, J' and D determined experimentally for both the Ni and Co compounds. An axial compression of the MS_4N_2 octahedra results in Ising-like anisotropy in both materials. As is typical, see [60], the anisotropy energy in the Co material is found to be considerably larger than in the Ni system.

Both compounds exhibit FM intrachain exchange, which is an order of magnitude greater in the Ni material than in the Co system. The electronic configurations, by identifying the semi-occupied (magnetic) orbitals shown in Table I, determine that in $Ni(NCS)_2(thiourea)_2$ only

a through-bond M—S—M exchange is possible, whereas in $Co(NCS)_2(thiourea)_2$ both through-bond M—S—M and through-space $M \cdots M$ magnetic interactions are available. As a result, in both materials spin-density extends along the thiourea bibridges (Figure 11), giving rise to strong FM exchange along the M—S—M pathways. However, the spin-density in the Co compound also extends directly along the a-axis, which leads to an additional AFM through-space interaction between Co ions. Competition between the two exchange pathways reduces the resultant intrachain exchange and explains the lower FM J in the Co system. This highlights the sometimes subtle ways in which the choice of transition metal ion affects the effective exchange strength. DFT calculations estimate the average interchain exchange to be around -0.1 K in both compounds in good agreement with magnetometry measurements.

$Ni(NCS)_2(thiourea)_2$ can be compared to the related material $NiCl_2(thiourea)_4$ (DTN), an AFM-coupled spin chain that contains two field-induced phase transitions that may belong to the universality class of BEC [10, 23]. Exchanging the Cl^- ion for the NCS^- ion causes a structural change from $I4$ for DTN [23] to $P\bar{1}$ in the present case, and the change in the local Ni(II) environment, from NiS_4Cl_2 to NiS_4N_2, has a strong effect on the SIA. The equatorial Ni—S bond lengths are similar in both systems: 2.46 Å for DTN and an average value of 2.57(3) Å for $Ni(NCS)_2(thiourea)_2$. However, the octahedra in DTN have a slight axial elongation with an equatorial to axial bond-length ratio of 0.98, while in $Ni(NCS)_2(thiourea)_2$ the octahedra are axially compressed with a bond-length ratio of 1.26. This results in the Ising-like SIA of $D \sim -10$ K, compared to the easy-plane SIA of $+8.12(4)$ K observed in DTN [10].

The lack of spatial-inversion-symmetry in DTN results in a net electric polarisation along the c direction [61]. In contrast, $Ni(NCS)_2(thiourea)_2$ does possess a centre of inversion symmetry, so we expect no net electric polarisation.

The structure and SIA of DTN is such that AFM exchange is mediated along linear Ni—Cl $\cdots$ Cl—Ni pathways [$J = -1.74(3)$ K] propagating along the c-

TABLE II. Comparison of the intrachain J, interchain J', and SIA D determined experimentally [$a = \chi(T)$, $b = M(H)$, $c = C_{mag}(T)$] and via DFT calculations. Negative exchange values indicate AFM interactions and negative D values indicate easy-axis behaviour. DFT values were calculated by considering a single J convention in the Hamiltonian where summations are made over unique exchange pathways.

	$Co(NCS)_2(thiourea)_2$			$Ni(NCS)_2(thiourea)_2$		
	J (K)	J' (K)	D (K)	J (K)	J' (K)	D (K)
Exp.	$3.62(7)^a$	$-0.3(1)^b$	$\sim -100^a$	$\sim 100^a$	$-0.13(1)^b$	$\sim -10^c$
DFT	4.22	-0.1	—	78.13	-0.1	—

axis. Within the *ab*-plane, non-bridging thiourea ligands keep the magnetic ions well separated (adjacent Ni sites are 9.595 Å apart), which results in weak AFM $J' = -0.17(1)$ K, possibly taking advantage of Ni—Cl$\cdots$(H$_2$N)$_2$—C—S—N superexchange pathways.

For Ni(NCS)$_2$(thiourea)$_2$, the thiourea ligands are no longer terminal but now connect adjacent Ni sites along *a* via Ni—S—Ni bibridges which mediate the large FM exchange along *a*. The thiourea ligands still keep adjacent Ni sites well separated along *b* at 7.527 Å, and H-bonding between the ligands mediates weak AFM J'. Although Ni—NCS—Ni bond pathways have been shown to effectively mediate magnetic exchange interactions in similar compounds [62], we find here that the NCS ligands are terminal and support only weak AFM J' via H-bonds along *c*. Thus, whilst DTN and Ni(NCS)$_2$(thiourea)$_2$ have highly similar equatorial environments, the dramatic structural change, invoked by substitution of the axial Cl$^-$ for NCS$^-$, leads to drastically different magnetic properties; from a Q1D *XY*-like AFM ground-state exhibiting QCP behaviour (DTN), to that of an FM coupled chain of Ising spins in Ni(NCS)$_2$(thiourea)$_2$.

Similarly, Co(NCS)$_2$(thiourea)$_2$ can be compared to the $S = 3/2$ analogue of DTN, CoCl$_2$(thiourea)$_4$ (DTC) [63]. DTC displays antiferromagnetic order below approximately 1 K that can be suppressed by magnetic fields of around 2 T, and somewhat surprisingly, the observed susceptibility and magnetisation are largely isotropic [61, 64]. Swapping the Cl$^-$ for NCS$^-$ ion results in a structural change, now from $P4_2/n$ to $P\bar{1}$. Average Co—S bond lengths in DTC and Co(NCS)$_2$(thiourea)$_2$ are equal to within errors at 2.53(3) Å and 2.57(3) Å, respectively. The local CoS$_4$N$_2$ environment is compressed along the axial N—Co—N bond such that the ratio of the equatorial Co—S to axial Co—N bond is 1.28, leading to a large Ising-like SIA $D \sim -100$ K. This contrasts with the isotropic behaviour seen in DTC which also possesses a slight axial compression, with a bond-length bond ratio of 1.02. Analogous to the comparison of the Ni species and DTN above, thiourea ligands form Co—S—Co bibridges in Co(NCS)$_2$(thiourea)$_2$ that mediate strong FM exchange along the *a*-axis, while the chains are well separated along *b*. Again NCS ligands are terminal and mediate weak AFM interactions along via H-bond networks along the *c*-axis.

Co(NCS)$_2$(thiourea)$_2$ can also be compared to the archetype transverse-field Ising chain material CoNb$_2$O$_6$, with both possessing strong Ising-like SIA with FM J and weak AFM J' [8]. Interchain exchange interactions induce a transition to long-range AFM order in both, at $T_c = 2.9$ K in CoNb$_2$O$_6$ [65] and $T_c = 6.82(5)$ K in Co(NCS)$_2$(thiourea)$_2$. The lower T_c for CoNb$_2$O$_6$ indicates a more ideal 1D system, with $J' \sim 0.01$ K [66] compared to 0.1 K for Co(NCS)$_2$(thiourea)$_2$. In CoNb$_2$O$_6$, a critical field applied perpendicular to the Ising-axis breaks the 3D-AFM order, pushing it through a QCP as

the material enters a quantum paramagnetic state [8, 9]. Because application of a transverse field consistently shattered Co(NCS)$_2$(thiourea)$_2$ single-crystals, we are as yet unable to provide evidence of similar quantum-critical behaviour in our material.

CONCLUSION

In summary, we find that M(NCS)$_2$(thiourea)$_2$, where $M =$ Ni(II) or Co(II), both behave as Q1D chains with ferromagnetic intrachain exchange J, weak antiferromagnetic interchain interactions J' and Ising-like single-ion anisotropy ($D < 0$). At low temperature, long-range AFM ordering is observed in both materials as confirmed by heat capacity, magnetometry and μ^+SR measurements. The considerable difference in the magnitude of J between the two compounds is due to their electronic configurations, where semi-occupied orbitals are responsible for the different spin-density distributions, highlighting the prominent role of the transition metal-ion in promoting Q1D behaviour. We find that the magnetic properties of the materials discussed here are very different to those observed in the chemically related quantum magnets DTN and DTC, owing to significant structural changes induced by substitution of the axial Cl$^-$ halide ion for the NCS$^-$ ion.

* p.goddard@warwick.ac.uk
† jmanson@ewu.edu

[1] S. Sachdev, Science **288**, 475 (2000).
[2] A. Vasiliev, O. Volkova, E. Zvereva, and M. Markina, npj Quantum Materials **3**, 18 (2018).
[3] T. Giamarchi, C. Rüegg, and O. Tchernyshyov, Nat. Phys. **4**, 198 (2008).
[4] F. D. M. Haldane, Phys. Rev. Lett. **50**, 1153 (1983).
[5] L. Savary and L. Balents, Reports on Progress in Physics **80**, 016502 (2016).
[6] J. M. Kosterlitz and D. J. Thouless, Journal of Physics C: Solid State Physics **6**, 1181 (1973).
[7] V. Zapf, M. Jaime, and C. D. Batista, Rev. Mod. Phys. **86**, 563 (2014).
[8] A. W. Kinross, M. Fu, T. J. Munsie, H. A. Dabkowska, G. M. Luke, S. Sachdev, and T. Imai, Phys. Rev. X **4**, 031008 (2014).
[9] R. Coldea, D. A. Tennant, E. M. Wheeler, E. Wawrzynska, D. Prabhakaran, M. Telling, K. Habicht, P. Smeibidl, and K. Kiefer, Science **327**, 177 (2010).
[10] V. S. Zapf, D. Zocco, B. R. Hansen, M. Jaime, N. Harrison, C. D. Batista, M. Kenzelmann, C. Niedermayer, A. Lacerda, and A. Paduan-Filho, Phys. Rev. Lett. **96**, 077204 (2006).
[11] S. A. Zvyagin, J. Wosnitza, C. D. Batista, M. Tsukamoto, N. Kawashima, J. Krzystek, V. S. Zapf, M. Jaime, N. F. Oliveira, and A. Paduan-Filho, Phys. Rev. Lett. **98**, 047205 (2007).
[12] J. Brambleby, P. A. Goddard, R. D. Johnson, J. Liu, D. Kaminski, A. Ardavan, A. J. Steele, S. J. Blundell, T. Lancaster, P. Manuel, P. J. Baker, J. Singleton, S. G. Schwalbe, P. M. Spurgeon, H. E. Tran, P. K. Peterson, J. F. Corbey, and J. L. Manson, Phys. Rev. B **92**, 134406 (2015).
[13] P. R. Hammar, M. B. Stone, D. H. Reich, C. Broholm, P. J. Gibson, M. M. Turnbull, C. P. Landee, and M. Oshikawa, Phys. Rev. B **59**, 1008 (1999).
[14] F. M. Woodward, A. S. Albrecht, C. M. Wynn, C. P. Landee, and M. M. Turnbull, Phys. Rev. B **65**, 144412 (2002).
[15] P. A. Goddard, J. Singleton, P. Sengupta, R. D. McDonald, T. Lancaster, S. J. Blundell, F. L. Pratt, S. Cox, N. Harrison, J. L. Manson, H. I. Southerland, and J. A. Schlueter, New J. Phys. **10**, 83025 (2008).
[16] P. A. Goddard, J. L. Manson, J. Singleton, I. Franke, T. Lancaster, A. J. Steele, S. J. Blundell, C. Baines, F. L. Pratt, R. D. McDonald, O. E. Ayala-Valenzuela, J. F. Corbey, H. I. Southerland, P. Sengupta, and J. A. Schlueter, Phys. Rev. Lett. **108**, 077208 (2012).
[17] J. Liu, S. Kittaka, R. D. Johnson, T. Lancaster, J. Singleton, T. Sakakibara, Y. Kohama, J. Van Tol, A. Ardavan, B. H. Williams, S. J. Blundell, Z. E. Manson, J. L. Manson, and P. A. Goddard, Phys. Rev. Lett. **122**, 57207 (2019).
[18] B. M. Huddart, J. Brambleby, T. Lancaster, P. A. Goddard, F. Xiao, S. J. Blundell, F. L. Pratt, J. Singleton, P. MacChi, R. Scatena, A. M. Barton, and J. L. Manson, Phys. Chem. Chem. Phys. **21**, 1014 (2019).
[19] R. C. Williams, W. J. A. Blackmore, S. P. M. Curley, M. R. Lees, S. M. Birnbaum, J. Singleton, B. M. Huddart, T. J. Hicken, T. Lancaster, S. J. Blundell, F. Xiao, A. Ozarowski, F. L. Pratt, D. J. Voneshen, Z. Guguchia, C. Baines, J. A. Schlueter, D. Y. Villa, J. L. Manson, and P. A. Goddard, Phys. Rev. Research **2**, 013082 (2020).
[20] G. Yagupsky, R. H. Negrotti, and R. Levitus, J. Inorg. Nucl. Chem. **27**, 2603 (1965).
[21] C. Puglisi and R. Levitus, J. Inorg. Nucl. Chem. **29**, 1069 (1967).
[22] M. Nardelli, G. F. Gasparri, G. G. Battistini, and P. Domiano, Acta Crystallographica **20**, 349 (1966).
[23] B. Figgis and P. Reynolds, Journal of The Chemical Society-dalton Transactions , 125 (1986).
[24] J. B. Goodenough, Phys. Rev. **100**, 564 (1955).
[25] J. Kanamori, J. Phys. Chem. Solids **10**, 87 (1959).
[26] R. Ivaniková, R. Boča, L. Dlhá, H. Fuess, A. Mašlejová, V. Mrázová, I. Svoboda, and J. Titiš, Polyhedron **25**, 3261 (2006).
[27] J. Titiš, R. Boča, L. Dlhá, T. určeková, H. Fuess, R. Ivaniková, V. Mrázová, B. Papánková, and I. Svoboda, Polyhedron **26**, 1523 (2007).
[28] J. Titiš and R. Boča, Inorg. Chem. **50**, 11838 (2011).
[29] See supplemental information at XXXXXXXX for experimental details and further analysis of μ^+SR, heat capacity and SCXRD.
[30] F. Pratt, Physica B: Condensed Matter **289**, 710 (2000).
[31] A. J. Steele, T. Lancaster, S. J. Blundell, P. J. Baker, F. L. Pratt, C. Baines, M. M. Conner, H. I. Southerland, J. L. Manson, and J. A. Schlueter, Physical Review B **84**, 064412 (2011).
[32] F. Xiao, J. S. Möller, T. Lancaster, R. C. Williams, F. L. Pratt, S. J. Blundell, D. Ceresoli, A. M. Barton, and J. L. Manson, Phys. Rev. B **91**, 144417 (2015).
[33] T. Lancaster, S. Blundell, M. Brooks, F. Pratt, and J. Manson, Physica B: Condensed Matter **374**, 118 (2006).
[34] J. L. Manson, C. M. Brown, Q. Huang, J. A. Schlueter, T. Lancaster, S. J. Blundell, J. Singleton, J. W. Lynn, and F. L. Pratt, Polyhedron **52**, 679 (2013).
[35] J. Liu, P. A. Goddard, J. Singleton, J. Brambleby, F. Foronda, J. S. Mller, Y. Kohama, S. Ghannadzadeh, A. Ardavan, S. J. Blundell, T. Lancaster, F. Xiao, R. C. Williams, F. L. Pratt, P. J. Baker, K. Wierschem, S. H. Lapidus, K. H. Stone, P. W. Stephens, J. Bendix, T. J. Woods, K. E. Carreiro, H. E. Tran, C. J. Villa, and J. L. Manson, Inorganic Chemistry **55**, 3515 (2016).
[36] J. J. Binney, N. J. Dowrick, A. J. Fisher, and M. E. Newman, *The Theory of Critical Phenomena: An Introduction to the Renormalization Group* (Oxford University Press, Oxford, 1992).
[37] J. C. Lashley, M. F. Hundley, A. Migliori, J. L. Sarrao, P. G. Pagliuso, T. W. Darling, M. Jaime, J. C. Cooley, W. L. Hults, L. Morales, D. J. Thoma, J. L. Smith, J. Boerio-Goates, B. F. Woodfield, G. R. Stewart, R. A. Fisher, and N. E. Phillips, Cryogenics (Guildf). **43**, 369 (2003).
[38] R. Honmura, Phys. Rev. B **30**, 348 (1984).
[39] X. Feng and H. W. J. Blöte, Phys. Rev. E - Stat. Nonlinear, Soft Matter Phys. **81** (2010).
[40] L. Onsager, Phys. Rev. **65**, 117 (1944).
[41] B. M. McCoy and T. T. Wu, *The Two-Dimensional Ising Model* (Harvard University Press, Cambridge MA, 1973).
[42] P. Baran, M. Boča, R. Boča, A. Krutošíková, J. Miklovič, J. Pelikán, and J. Titiš, Polyhedron **24**, 1510 (2005).
[43] J. Titi and R. Boça, Inorg. Chem. **49**, 3971 (2010).
[44] M. E. Fisher, Philos. Mag. **7**, 1731 (1962).

[45] M. E. Fisher, J. Math. Phys. **4**, 124 (1963).
[46] R. E. Greeney, C. P. Landee, J. H. Zhang, and W. M. Reiff, Phys. Rev. B **39**, 12200 (1989).
[47] M. E. Lines, J. Chem. Phys. **55**, 2977 (1971).
[48] F. Lloret, M. Julve, J. Cano, R. Ruiz-García, and E. Pardo, Inorganica Chim. Acta **361**, 3432 (2008).
[49] Phys. Chem. Chem. Phys. **19**, 3232 (2017).
[50] W. J. A. Blackmore, J. Brambleby, T. Lancaster, S. J. Clark, R. D. Johnson, J. Singleton, A. Ozarowski, J. A. Schlueter, Y.-S. Cheng, A. M. Arif, S. Lapidus, F. Xiao, R. C. Williams, S. J. Blundell, M. J. Pearce, M. R. Lees, P. Manuel, D. Y. Villa, J. A. Villa, J. L. Manson, and P. A. Goddard, New J. Phys. **21**, 093025 (2019).
[51] P. Macchi, H.-B. Bürgi, A. S. Chimpri, J. Hauser, and Z. Gál, J. Appl. Crystallogr. **44**, 763 (2011).
[52] "Crysalispro," CrysAlisPRO, Oxford Diffraction /Agilent Technologies UK Ltd, Yarnton, England.
[53] G. M. Sheldrick, Acta Crystallographica Section C **71**, 3 (2015).
[54] A. Valkov, P. Macchi, L. J. Farrugia, C. Gatti, P. Mallinson, T. Richter, and T. Koritsanszky, "XD2016," (2016).
[55] N. K. Hansen and P. Coppens, Acta Crystallographica Section A **34**, 909 (1978).
[56] A. Holladay, P. Leung, and P. Coppens, Acta Crystallographica Section A **39**, 377 (1983).
[57] R. Dovesi, R. Orlando, A. Erba, C. M. Zicovich-Wilson, B. Civalleri, S. Casassa, L. Maschio, M. Ferrabone, M. De La Pierre, P. D'Arco, Y. Noël, M. Causà, M. Rérat, and B. Kirtman, Int. J. Quantum Chem. **114**, 1287 (2014).
[58] M. F. Peintinger, D. V. Oliveira, and T. Bredow, Journal of Computational Chemistry **34**, 451 (2013).
[59] R. F. W. Bader, Chemical Reviews **91**, 893 (1991).
[60] R. Boča, Coord. Chem. Rev. **248**, 757 (2004).
[61] E. Mun, J. Wilcox, J. L. Manson, B. Scott, P. Tobash, and V. S. Zapf, Adv. Condens. Matter Phys. **2014**, 512621 (2014).
[62] J. Palion-Gazda, B. Machura, F. Lloret, and M. Julve, Cryst. Growth Des. **15**, 2380 (2015).
[63] J. E. O'Connor and E. L. Amma, Inorganic Chemistry **8**, 2367 (1969).
[64] H. Forstat, N. D. Love, J. McElearney, and H. Weinstock, Phys. Rev. **145**, 406 (1966).
[65] W. Scharf, H. Weitzel, I. Yaeger, I. Maartense, and B. M. Wanklyn, J. Magn. Magn. Mater. **13**, 121 (1979).
[66] T. Kunimoto, K. Nagasaka, H. Noriji, S. Luther, M. Motokawa, H. Ohta, T. Goto, S. M. Okubo, and K. Kohn, J. Phys. Soc. Japan **68**, 1703 (1999).